Research Square

Preprints are preliminary reports that have not undergone peer review.
They should not be considered conclusive, used to inform clinical practice,
or referenced by the media as validated information.

Auditable Finite-Window Interface Qualification for Inverter Control and Relay Measurements

Sen Fu

fs211314@gmail.com

Changsha Vocational Technical College

Yan Fu

XJ Electric Co., Ltd.

Article

Keywords: inverter-based resources, relay measurement, interface contract, virtual impedance, uncertainty propagation

Posted Date: November 24th, 2026

DOI: https://doi.org/10.21203/rs.3.rs-11590379/v1

License: This work is licensed under a Creative Commons Attribution 4.0 International License.
Read Full License

Additional Declarations: No competing interests reported.

Auditable Finite-Window Interface Qualification for Inverter Control and Relay Measurements

Sen Fu[1*] and Yan Fu[2]

[1*]Changsha Vocational And Technical College, Changsha, Hunan, China.
[2]XJ Electric Co., Ltd., Xuchang, Henan, China.

*Corresponding author(s). E-mail(s): fs211314@gmail.com;
Contributing authors: fuyan1213@126.com;

Abstract

Time-varying inverter control and finite-window relay measurements can represent different quantities despite nominally identical impedances, which creates an interface problem for any compensated measurement compared across implementations. We propose an auditable qualification ledger that separates coefficient exchange, inductor endpoints and actuator realization, and propagates bounded telemetry uncertainty through the exchange calculation. At a system frequency of 50 Hz, numerical closure coverage within the declared working domain is 100.0%, the median residual is 2.05e-05 per unit (p.u.), and the median paired full-to-frozen residual ratio is 0.001448. A same-information scalar experiment gives narrower reachable-dynamics intervals than a range-clipped rate bound while retaining sampled containment. The averaged-source sweep retains all 108 physical configurations, of which 10 satisfy the original 1.5-p.u. current and 1.2-p.u. voltage domain. A causal sampled-data follow-up retains 108/108 tuples under readback delay, bounded perturbations, parameter mismatch and actuator lag, with peak current 1.4778 p.u.; an added 2-ms detection delay retains only 3/108. An independent uncalibrated three-phase stress audit retains 0/18 held-out tuples and activates in 3/6 nonfault cases. Both are model-conditional: numerical closure is not protection security, dependability, selectivity or hardware validation.

Keywords: inverter-based resources, relay measurement, interface contract, virtual impedance, uncertainty propagation

1 Introduction

Grid-forming inverters with current-limiting control shape fault currents differently from synchronous machines, and this difference propagates into protection behaviour [1, 2]. Reported sensitivities span the current-limiting strategy, the prefault operating point, converter settings, fault type and fault-current injection policy [3–9]. Virtual-impedance-based fast current injection, nonlinear transient virtual impedance, post-fault power-angle resetting and grid-code current requirements all change the impedance a relay sees during the fault [10–16]. Adaptive virtual-impedance schemes have been proposed specifically to shape fault response and reactive current [17–20]. Exchanging an impedance value is therefore insufficient: controller and relay must also agree on physical port, waveform history, time reference and actuator realization.

Adaptive and analytical protection schemes have been proposed for inverter-dominated networks [21–28]. Maturity analyses of protection solutions near inverter-based resources note that many proposals remain at the simulation or conceptual stage [29]. Protection-interoperable fault-ride-through control adjusts inverter power control to preserve incremental-quantity supervising elements [30]. Related research addresses superimposed distance protection [31], coordination of distance protection and current control [32], directional and pilot elements [33, 34], and control–protection coordination strategies for converter-connected lines [35, 36]. The present question concerns the measurement interface used by such designs: which terms and uncertainty information must accompany a time-varying controller quantity when it is evaluated through a finite window at another physical port?

On the measurement side, phasor and impedance estimation under transient conditions depend on the observation window, the demodulation convention and compensation of dynamic phase error [37–40]. Impedance-based fault-location studies compare fixed and variable data windows and local-measurement formulations [41–44]. Those works treat the estimator as the object of design. The present study instead treats the *interface record* that must accompany a controller-supplied quantity before any such estimator is applied.

The mathematical ingredients have established precedents. Generalized averaging represents waveforms by sliding-window Fourier coefficients and gives differentiation and product rules [45]. Set-membership and bounded-error estimation propagate regions containing a state under bounded disturbances, including power-system state estimation and corrupted measurements [46–50]. Model invalidation tests whether observations are compatible with an uncertain model; Harirchi and Ozay formulate this consistency problem for hidden-mode switched affine systems and establish finite-horizon detectability conditions [51]. Active fault-detection methods design inputs so that inconsistency becomes observable [52]. Here these ideas are specialized to an explicit controller–measurement interface: the object bounded is the coefficient-exchange error, the information constraint is aged controller readback, and the output is qualification of a particular compensation calculation. Table 1 distinguishes these objects from the adjacent tasks.

For a linear window $\mathcal{F}$, coefficient z, and aligned current increment d, replacing $\mathcal{F}[zd]$ by $z_k\mathcal{F}[d]$ creates an exchange term. Physical inductance additionally contributes a finite-window endpoint, and a constrained actuator contributes a realization

Table 1 Position relative to selected, full-text-inspected methodological and application precedents. The comparison concerns the stated problem and output, not comparative protection performance.

Precedent	Established object and method	Object addressed in this study
Generalized averaging [45]	Sliding-window Fourier coefficients, differentiation, and products	Port-specific exchange, endpoint, and actuator contributions to a measurement residual
Set-membership filtering [46]	State-containing ellipsoids with bounded noise and outlier detection	Controller-coefficient intervals propagated through the exchange calculation
Model invalidation [51]	Feasibility of input–output traces and model-based fault detectability	Qualification of a compensated measurement under explicit domain and error budgets
Protection-interoperable control [30]	Controller redesign to preserve supervising elements, with hardware evidence	Readback and waveform requirements for a controller–relay measurement interface

residual. These terms can cancel, so a small total residual alone does not identify a valid interface.

The problem addressed here is therefore interface qualification rather than protection performance: given a compensated measurement computed at one physical port from a time-varying controller quantity, what must be recorded and bounded before that measurement may be admitted as evidence? We propose a *decompose–bound–qualify* chain aimed at producing admissible interface evidence rather than an unqualified compensation number. First, a port-consistent finite-window decomposition separates coefficient exchange, the physical-inductor endpoint, and actuator realization, making cancellation between implementation errors observable. Second, controller-aware propagation maps telemetry age into both rate-based and reachable-dynamics bounds under matched information, including a range-clipped rate comparison that isolates the value of dynamics from simple recentering. Third, the resulting error budget defines ADMISSIBLE, MARGINAL, INVALID and NOT_ASSESSED interface states (Supplementary Table S1) so that a relay-side calculation can either be admitted with a bounded error radius or rejected with an explicit reason. This gives a reproducible interface-qualification methodology: the positive claim is not that every tested controller setting is usable, but that usable settings and non-actionable measurements become distinguishable by the same computable contract.

The numerical study reports the original qualification envelope, an ideal feedforward reference and a causal sampled-data sensitivity follow-up on the same physical grid. The latter tests sensor delay, finite correlated perturbations, source-parameter mismatch, actuator lag, detection latency and requested current, separating a realizable sampled implementation from the ideal cancellation reference. An independent, uncalibrated three-phase circuit stress audit is reported as an exploratory adverse check rather than as confirmatory evidence.

2 Results

Table 2 Primary physical-sweep states and denominators

State	Records	Percentage
ADMISSIBLE	0	0.0%
MARGINAL	0	0.0%
INVALID	1470	90.7%
NOT_ASSESSED	150	9.3%
Total age/phase records	1620	100.0%
Unique physical configurations	108	—

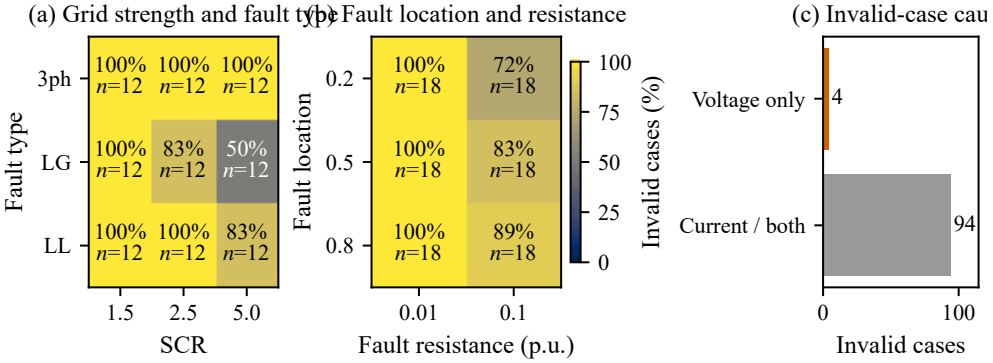

Fig. 1 Physical working-domain audit. Cells show failure rates and numbers of unique physical configurations, without rotation or age duplication. Panel (c) partitions failures into voltage-only and current-involving violations. Both heatmaps use the same percentage scale.

2.1 Working-domain qualification and conditional closure

The interface ledger produces two complementary outcomes: positive closure evidence inside its declared domain and explicit refusal outside it. Of 108 physical configurations, 10 satisfy the declared current–voltage domain. Figure 1 reports the remaining domain rejections with unique physical configurations as the denominator; the record-level state counts are given in Table 2. These rejections are useful qualification outcomes: they prevent a saturated voltage command or command-level current limit from being misread as a bounded relay-bus measurement. The primary sweep has 98/108 physical tuples (90.7%) with a direct domain violation and 10/108 with no physical violation but without a complete interface budget or calibrated decision margin. With 15 rotation/age records per tuple, the corresponding record-level state counts are 1470 INVALID, 150 NOT_ASSESSED, and zero ADMISSIBLE or MARGINAL; the additional records are deterministic conditions, not independent configurations. Conditional on the 10 valid configurations, numerical closure coverage is 100.0% and median closure is 2.05e-05 p.u. The full-to-frozen median paired ratio is 0.001448. These values support the positive implementation claim: when the physical-domain assumptions hold, the ledger closes the same sampled trajectories far more tightly than the frozen-product proxy. The main sweep contains 1470 domain-INVALID records and 150 NOT_ASSESSED records. The latter have valid physical

domains but lack a complete interface error budget and calibrated downstream margin; they are retained as candidate cases for margin design, not counted as protection permissions.

Supplementary Table S3 makes the retained working envelope explicit. All 10 tuples have fault resistance 0.1 p.u.; none is at SCR=1.5, two are at SCR=2.5 and eight at SCR=5.0. The retained fault types are eight LG and two LL cases, with no retained 3ph case; five, three and two retained tuples are at locations 0.2, 0.5 and 0.8, respectively. These counts describe this deterministic grid and are not estimates of deployment prevalence. Across the admitted-by-domain tuples, the maximum source-current and relay-bus-voltage magnitudes are 1.4334 p.u. and 1.1903 p.u., respectively, under the 1.5-p.u. and 1.2-p.u. domain limits. The tuples remain NOT_ASSESSED for downstream protection admission because a complete calibrated budget and margin are absent.

2.2 Follow-up domain-governor envelope

Supplementary Table S4 reports the per-topology domain counts for this follow-up.

The follow-up source-current domain governor keeps 108 of 108 physical tuples inside the declared current–voltage domain, reducing the physical-domain invalid fraction to 0.0%. The maximum observed source-current and relay-bus-voltage magnitudes are 0.4500 p.u. and 1.0372 p.u., respectively. Ledger closure remains below 4.475e-16 p.u. over the retained primary tuples. These results describe an ideal feedforward feasibility benchmark under the assumptions in the numerical design, while still requiring downstream relay margins before any tripping permission is inferred.

The same physical tuples, limits and ledger checks are retained. The 108-of-108 domain retention establishes feasibility under the ideal feedback-cancellation assumptions defined above. It does not establish performance with measurement imperfections or detection delays.

2.3 Nonideal causal domain sensitivity

Supplementary Table S5 lists all ten conditions with their retained counts, peak magnitudes and command-clipping fractions.

The complete follow-up contains 2376 condition runs, including 216 fixed step-refinement runs, with no execution failures. The combined condition retains 108 of 108 physical tuples, with sampled peak current 1.4778 p.u. and bus voltage 1.0575 p.u. Thus the enlarged domain is not restricted to exact instantaneous cancellation in this model. The margin remains finite and delay-dependent: an additional 2-ms detector delay retains only 3 tuples, whereas the 0.9-p.u. current-request condition retains 105. Figure 2 shows these boundaries rather than pooling them into an overall success rate.

Halving the step for the combined condition changes current and voltage peaks by at most 0.00704 p.u. and 0.001352 p.u., respectively, with 0 domain-flag changes across 216 matched conditions. A separate matrix-exponential integration of the same piecewise-linear plant and held command retains all 216 combined conditions,

with maximum current 1.4847 p.u., maximum voltage 1.0591 p.u. and 0 classification changes. These checks support the reported sampled classification; they are not continuous-time worst-case guarantees.

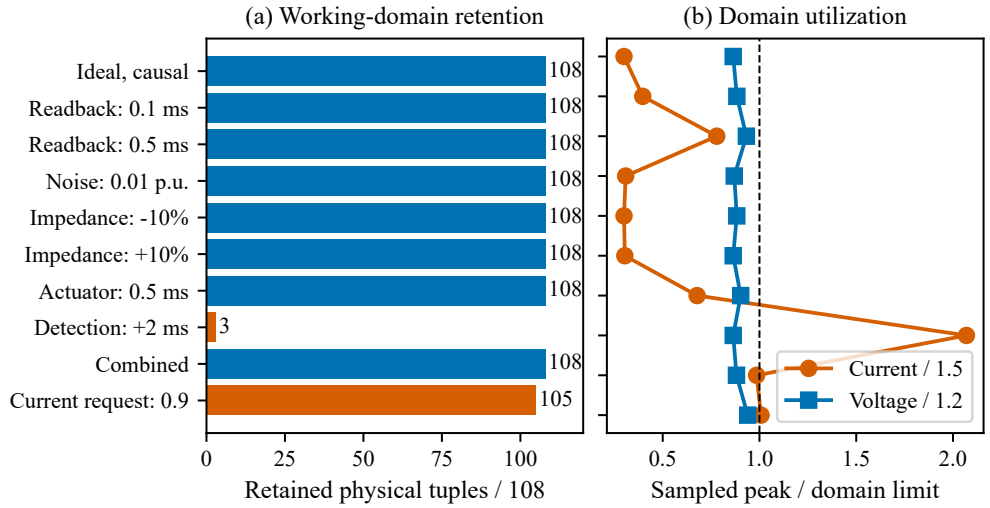

Fig. 2 Causal controller sensitivity over the matched physical grid. (a) Physical tuples satisfying both deterministic phase conditions. (b) Maximum sampled current and bus-voltage magnitudes, divided by their respective domain limits; the dashed line is the limit. These are finite-grid sensitivities, not deployment probabilities.

2.4 Three-phase audit outcomes

The independent three-phase circuit audit does not reproduce the strong domain retention observed in the separately specified causal follow-up. The frozen training rule selects zero restoring gain: domain retention is 3/36 at zero gain and 0/36 at each tested positive gain. On the held-out tuples, both the selected zero-gain policy and the matched zero-gain reference satisfy the full-history current–voltage limits in 0/18 cases. Thus, this audit provides no evidence that the tested gain improves held-out domain retention. The local detector activates in 3/6 nonfault cases (the two load steps and the 10-degree phase jump), while it does not activate for either voltage sag or the 5-degree phase jump. These results indicate limited selectivity under the tested disturbances, not a validated relay false-trip rate.

For a representative held-out case (3ph, SCR=1.5, $R_f = 0.01$ p.u., location 0.8), the fault-on voltage peak is 1.063 p.u.; the sampled post-clear voltage peak is 7.193 p.u. at approximately 0.542 ms after clearing, and the sampled current peak is 3.102 p.u. Repeating this case at a 1-μs output interval changes the post-clear voltage peak by less than 0.001 p.u. This step check addresses output-grid sensitivity only. The high peak is a model-conditional adverse result; without device-parameter calibration and independent electromagnetic-transient (EMT)/hardware comparison, it must not be interpreted as a quantitative prediction for a deployed inverter. Complete records and

scope limitations are documented in the accompanying phase-domain audit report. The cross-model discrepancy was further examined with a post-hoc mechanism diagnostic on one held-out three-phase tuple. The diagnostic is not used for gain selection or confirmatory coverage. With the fault cleared at 60 ms, the post-clear sampled voltage peak is 7.193 p.u.; moving clearing to 65 ms and 70 ms reduces it to 4.071 and 3.877 p.u., respectively. At a clearing time of 80 ms or later, the 80-ms record contains no post-clear interval, so no post-clear peak is reported for those cases. Scaling the bus capacitance by 0.25, 0.5, 1 and 2 gives post-clear voltage peaks of 11.132, 9.015, 7.193 and 5.643 p.u. The pattern is consistent with fault clearing interacting with the uncalibrated dynamic energy-storage and damping assumptions, but it does not isolate a unique physical cause or validate the parameter values. (Supplementary Fig. S1)

2.5 Complex-residual implementation comparison

Table 3 compares the same sampled signals through five residual definitions. Endpoint and actuation terms are added as complex quantities before taking magnitudes. The valid subset shows that the endpoint-aware and full ledgers align at the reported precision for these trajectories, so the dominant improvement over the frozen-product proxy comes from using the physical window and endpoint convention consistently. Figure 3 displays the paired ratios, including outliers. The small full-ledger residual is a positive consistency result for the interface calculation; downstream relay-performance claims require a separately calibrated decision statistic.

Table 3 Conditional residual medians over unique valid configurations

Implementation	Median residual (p.u.)
Frozen coefficient	0.01535
Waveform product	0.006237
Delayed coefficient	0.01531
Waveform plus endpoint	2.05e-05
Full physical ledger	2.05e-05

2.6 Numerical and telemetry cross-checks

The adaptive-reference comparison and the separately planned bounded-telemetry experiment are reported below. Their source arrays, protocols and executable checks accompany the manuscript. An adaptive DOP853 reference with a separately restated right-hand side cross-checks the fixed-step Heun implementation. Supplementary Table S6 reports maximum current error over each trajectory. The near fourfold error reduction when halving the step is consistent with second-order convergence. Both solvers share the network equations, so this checks numerical implementation rather than physical model validity.

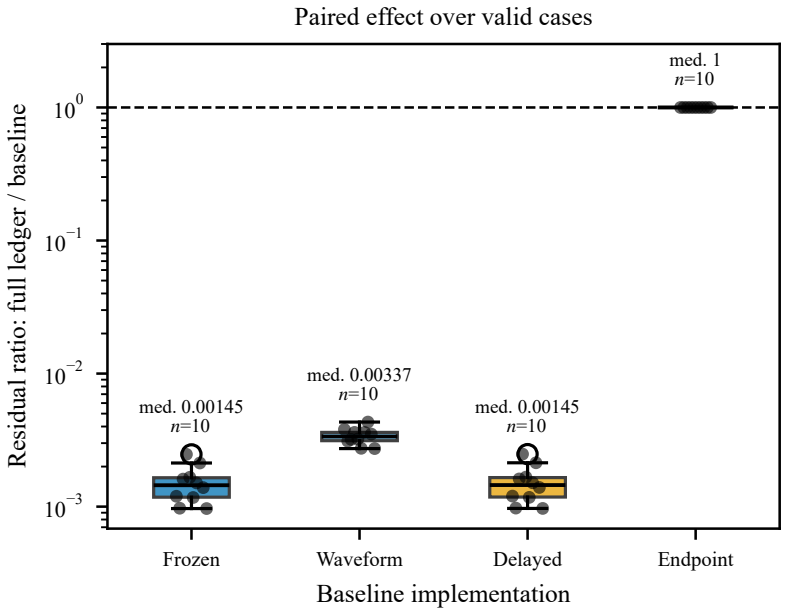

Fig. 3 Paired full-ledger/baseline residual ratios over unique domain-valid configurations on a logarithmic axis. Points show all configurations; boxes show empirical quartiles, lines show medians, and whiskers terminate at observations within 1.5 interquartile ranges. The dashed line marks equal residuals. These are descriptive finite-grid distributions.

The bounded-telemetry primary grid contains 65 exact scalar trajectories and 3510 trajectory–age–noise conditions per method. Both bounded methods contain all sampled correction values, with zero false-safe margin violations. Mean radii are 0.9872 p.u. for the clipped rate bound and 0.7304 p.u. for the reachable bound. Nevertheless, both classify every condition as INVALID under the declared allocation. A narrower interval alone therefore does not establish a usable interface.

After observing this outcome, an explicitly post-hoc exploratory grid reduced ages to 0–0.1 ms while retaining the budget and margin. Reachable intervals give 817 ADMISSIBLE, 989 MARGINAL and 1704 INVALID conditions; the corresponding clipped-rate counts are 581, 783 and 2146. Both retain complete sampled containment and zero false-safe violations. These are synthetic margin diagnostics, not measured relay operations. Figure 4 separates the planned and exploratory results.

The maximum exchange change on halving the quadrature step is 0.001125 p.u. This is a sensitivity observation, not a certified integration bound; reported interval coverage and decisions refer to the sampled operator. Repeated noise/age conditions on one trajectory are not independent replications.

For the 3510 matched primary-grid conditions, the reachable interval is narrower than the range-clipped rate interval in all cases. The reachable-to-rate radius ratio has median 0.6437 (IQR 0.4926–0.9196); its absolute-radius reduction has median 0.1139 p.u. (range 0.0016–0.8582 p.u.). Both methods nevertheless classify all 3510 conditions as INVALID under the declared 0.05-p.u. allocation, with zero false-safe margin

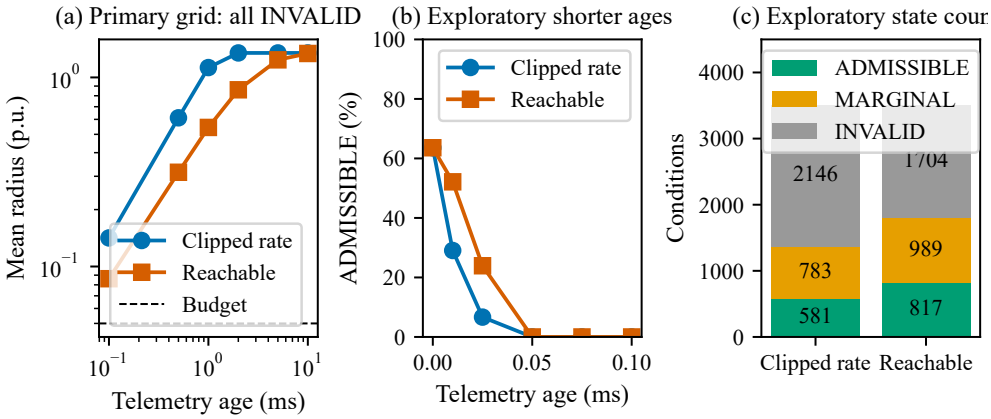

Fig. 4 Same-information bounded-telemetry comparison. (a) Mean radius over the primary stress grid, with the allocation shown. (b) Fraction of conditions qualified on the explicitly exploratory shorter-age grid. (c) Counts over all exploratory trajectory–age–noise conditions. Curves summarize a deterministic grid; they are not population estimates.

violations. The comparison therefore establishes a tighter bound under matched information, not an improved engineering qualification rate or a more accurate estimate against an external truth.

3 Discussion

The practical contribution is a qualification record for waveform history, coefficient age, physical endpoints and applied actuation. Its algebra identifies which information must be retained before a compensated measurement can be compared across implementations, and its state labels convert that information into an auditable admission decision. The bounded-telemetry experiment gives a constructive positive result: with the same aged readback and current information, reachable-dynamics bounds are tighter than a range-clipped rate comparator while retaining sampled containment. The physical sweep demonstrates the complementary safety function of the same contract: operating conditions outside the declared current–voltage domain are rejected before they can be interpreted as protection evidence.

Within the valid working subset, the low full-ledger residual establishes consistency between the sampled model equations and the retained implementation. This is the evidence needed for interface qualification: the finite-window calculation, endpoint convention and actuation record agree on the same physical quantity. A useful downstream trip decision additionally requires a calibrated statistic and a defensible error allocation. The present physical sweep therefore identifies both a verified interface calculation in its declared domain and a concrete engineering target for the next controller design: enlarge the set of configurations that remain inside the current–voltage domain without changing the qualification thresholds after the fact.

The source-current benchmark defines an exact-cancellation reference, while the new causal sampled-data study tests whether domain retention survives specific implementation imperfections. It does under the combined condition, with peak current

1.4778 p.u. against the 1.5-p.u. limit, but deteriorates sharply under an additional 2-ms detection delay. The 0.9-p.u. requested-current case also causes some domain rejections and actuator clipping. Thus, current-domain retention depends on detection, actuation and requested support, rather than on the controller formula alone. The measured local threshold removes oracle fault timing from this follow-up without establishing a complete protection detector.

The separate three-phase averaged RL-C stress audit qualifies that positive result: it uses a different, more dynamically resolved but uncalibrated circuit and does not confirm the high retention found in the original causal follow-up. It selects zero gain, retains 0/18 held-out tuples inside the declared domain, and activates on 3/6 tested nonfault disturbances. Its large post-clear voltage excursion is numerically insensitive to the tested output-step refinement but remains structurally and parametrically unvalidated. The two simulation studies therefore support model-specific conclusions only; they do not jointly establish a robust physical operating envelope. In particular, the favorable retention in the causal follow-up should not be generalized beyond its declared plant and disturbance family.

These outcomes are not a paired cross-model performance comparison. The primary causal follow-up retains a dynamic source branch connected to a quasi-steady external network, uses its original 108-tuple radial/meshed grid and fault-admittance proxies, and evaluates the source-current governor with sampled nonidealities. The independent circuit instead adds dynamic line-current states and shunt bus capacitances, uses explicit three-phase, phase-to-ground and phase-to-phase fault connections over 54 different tuples, and evaluates a separate local-detector/restoring-gain law. The per-unit fault, controller, parameter and operating-point mappings have not been calibrated to make these tests physically equivalent. Therefore 108/108 and 0/18 are evidence for different declared models and protocols, not commensurate estimates of a single controller's transfer loss. The post-hoc clearing-time and capacitance diagnostics identify a model-conditional mechanism but do not isolate every cause; a matched, device-calibrated cross-model experiment remains necessary before quantitative physical attribution.

The primary physical sweep combines an averaged source RL branch with a quasi-steady external network. The adaptive solver comparison checks numerical implementation of this same model. The independent phase-domain audit adds dynamic line currents, shunt capacitances and unbalanced fault connections, but its component parameters and controller are not calibrated against a device or independent EMT reference; its adverse result is a model-conditional stress finding rather than a physical prediction. The scalar telemetry experiment studies a declared first-order controller and bounded measurement errors, so its state transitions establish a mechanism under those assumptions. Extending the qualification to transformer zero-sequence behavior, switching EMT, controller-hardware-in-the-loop (CHIL) or field waveforms requires the same ledger fields to be recomputed on calibrated evidence sources. The nonideal follow-up uses one disturbance frequency, two phases, a fixed detection threshold and a finite set of parameter offsets. It establishes a sampled sensitivity envelope, not worst-case robustness over arbitrary disturbances. Packet loss,

timing jitter, frequency-estimation error, continuous-time peak guarantees and a complete measured sensor/actuator error budget remain outside that envelope. Detection is latched through clearing; reset and reclosing logic require a separate design.

The finite parameter grid is a coverage design, not a random sample of a deployment population. Rotations test a symmetry; ages change the measurement problem. Treating either as independent replication would exaggerate precision. The retained code distinguishes physical configurations, measurement conditions and unique evidence identifiers. A complete relay comparison would further require pickup, persistence, selectivity and operating-time criteria; this interface study is not a tripping algorithm, but it supplies the measurement-side evidence that such a comparison should consume. The telemetry comparison bounds the proposed interval against generic rate-based and recentred rate-based comparators only. No production phasor estimator, such as a discrete-Fourier or least-squares relay estimator, was implemented or run as a comparator, so the reported tightening is a statement about these declared bounds and not a benchmark against deployed estimator designs.

In conclusion, a controller-side compensation and a finite-window measurement can be qualified when the physical port, prefault reference, window, coefficient history, endpoint convention and realized actuation are all part of the same interface record. The proposed ledger makes those dependencies computable. In the verified working subset it closes the model residual to 2.05e-05 p.u. and separates the full physical ledger from a frozen-product proxy by a median paired ratio of 0.001448. The same-information telemetry comparison provides a constructive way to reduce uncertainty radii before a measurement is admitted. The ideal feedforward benchmark establishes an exact-model reference. The causal sampled-data follow-up retains 108 of 108 tuples under the specified combined imperfections; an additional 2-ms detector delay reduces retention to 3 of 108. These results identify detection latency as a material domain constraint in this model. Together, they support the paper's central claim: finite-window compensation should be admitted through an auditable interface state, not through a bare impedance exchange or an unqualified residual. Future work should combine this interface contract with electromagnetic-transient, controller-hardware-in-the-loop, or hardware evidence and calibrated protection margins for security, dependability, selectivity, and operating time.

A separate uncalibrated three-phase stress audit retained 0/18 held-out tuples in the declared domain and activated in 3/6 nonfault cases. It does not confirm the favorable retention of the primary causal follow-up; the two results are specific to their declared simulation models and do not establish hardware-level robustness.

4 Methods

4.1 Problem Formulation: Physical Port and Measurement Interface

4.1.1 Port, polarity, and increment definitions

The source branch connects an averaged controlled voltage u to relay bus A through resistance R_s and inductance L_s. The source current i_s enters A; the line current

i_l leaves A toward the protected branch. They differ by the bus shunt current, particularly for a reverse bus fault. Figure 5 fixes these polarities and the information path. The finite-window demodulation used throughout is defined in (3). In balanced stationary $\alpha\beta$ coordinates, complex variables use root-mean-square (RMS)-normalized orthogonal components. Define the aligned increment $d = i_s - i_{s,\mathrm{pre}}$ and $\Delta v_A = v_A - v_{A,\mathrm{pre}}$, where each prefault quantity is extrapolated in the same frame and at the same frequency as its corresponding waveform. For the ideal template, assume $e_{\mathrm{pre}} - v_{A,\mathrm{pre}} = R_s i_{s,\mathrm{pre}} + L_s \dot{i}_{s,\mathrm{pre}}$. Subtracting this prefault Kirchhoff's voltage law (KVL) gives

$$\Delta v_A = -R_s d - L_s \dot{d} - z d + p, \tag{1}$$

where the defined actuator residual is

$$p = (u - e_{\mathrm{pre}}) + z d. \tag{2}$$

Thus the actuator term in (2) vanishes, $p = 0$, for an ideal source implementing $u = e_{\mathrm{pre}} - z d$. A nonzero prefault KVL defect $r_0 = e_{\mathrm{pre}} - v_{A,\mathrm{pre}} - R_s i_{s,\mathrm{pre}} - L_s \dot{i}_{s,\mathrm{pre}}$ must be added separately to (1), not hidden inside actuation. Finite tracking bandwidth and voltage limiting generally make $p \neq 0$. The sign in (1) is fixed by the branch polarity; it is not a selectable compensation convention. In the three-phase model the corresponding relation is vector-valued with algebraic matrix $K(t)$ in place of $z(t)$.

Equation (1) holds under either fault direction. It is a consistency equation, not a classifier; a protective element additionally needs a physical voltage–line-current relation and its own pickup and trip logic.

4.1.2 Continuous and discrete windows

Following the generalized-averaging convention of sliding-window Fourier coefficients [45], for a rectangular physical-time demodulation window of duration T,

$$\mathcal{F}_t[x] = \frac{1}{T} \int_{t-T}^{t} x(\tau) e^{-\mathrm{j}\omega\tau} \, \mathrm{d}\tau. \tag{3}$$

Integration by parts yields

$$\mathcal{F}_t[\dot{d}] = \mathrm{j}\omega D_t + H_t, \quad D_t = \mathcal{F}_t[d], \tag{4}$$

$$H_t = \frac{d(t) e^{-\mathrm{j}\omega t} - d(t-T) e^{-\mathrm{j}\omega(t-T)}}{T}. \tag{5}$$

The endpoint contribution vanishes when the demodulated endpoint values in (5) agree, for example for a settled sinusoidal increment at the demodulation frequency; ordinary periodicity alone is insufficient. A virtual reactance implemented as a cross-axis multiplication is not interchangeable with the physical derivative in (4).

The numerical audit uses composite trapezoidal demodulation: $N = T/h$ intervals, $N + 1$ samples, and half endpoint weights. Its discrete operator $\mathcal{F}_k[x] = \sum_j w_{kj} x_j$

has an exact coefficient-exchange identity, but physical KVL closure retains quadrature error checked by refining h. This differs from the original N-sample rectangular average.

4.1.3 Information interface and native endpoint

The offline verification uses sampled source and line currents, bus voltage, actual applied source voltage, a prefault template, and controller coefficient histories. The telemetry analysis withholds contemporaneous coefficients from its estimator: only delayed coefficients, an age upper bound, declared controller dynamics, and noisy current increments are available. Fault labels and remote fault current are never used to construct the bound. Clean waveforms are used only as offline reference values.

With aligned, calibrated voltage/current readbacks and the stated prefault template, p is reconstructible up to their propagated errors. If an implementation exposes only a command, an independent actuator-error bound is required. Without that readback or bound the full error ledger is incomplete; an exchange-only interval must not be advertised as a total voltage-error interval. Our native endpoint is consequently *interface consistency at the relay bus*, measured through the residual of (1), not protective security, dependability, or clearing time.

4.2 Method: A Composable Interface Error Budget

4.2.1 Physical-port error ledger

Let $A = \mathcal{F}[zd]$, $D = \mathcal{F}[d]$, and $V = \mathcal{F}[\Delta v_A]$. Define the exchange term and actuator term by

$$C_k = A_k - z_k D_k = \sum_j w_{kj}(z_j - z_k)d_j, \tag{6}$$

$$P_k = \mathcal{F}_k[p]. \tag{7}$$

For the continuous operator, (1)–(5) give the exact ledger

$$E_{\mathrm{f}} := V + (R_s + \mathrm{j}\omega L_s + z_k)D = -C - L_s H + P. \tag{8}$$

The matched implementations of (6) are now unambiguous: the frozen-product residual is E_{f}; replacing its product by the waveform product gives $E_{\mathrm{w}} = E_{\mathrm{f}} + C$; accounting for the endpoint gives $E_{\mathrm{b}} = E_{\mathrm{w}} + L_s H$; incorporating actual actuation gives $E_{\mathrm{c}} = E_{\mathrm{b}} - P$. Discretization leaves a numerical closure residual E_{c} that is checked by refinement. In particular, (8) shows that $V + C$ alone is not the matched replacement of a frozen *compensated* voltage by its waveform-product counterpart.

The ledger components should be assessed together. A nonzero E_{w} can be due to endpoints or actuation, and a small E_{f} can hide cancellation between large components. In E_{c} the coefficient cancels, so closure does not independently validate telemetry. The same-data comparisons are implementation ablations, not named relays.

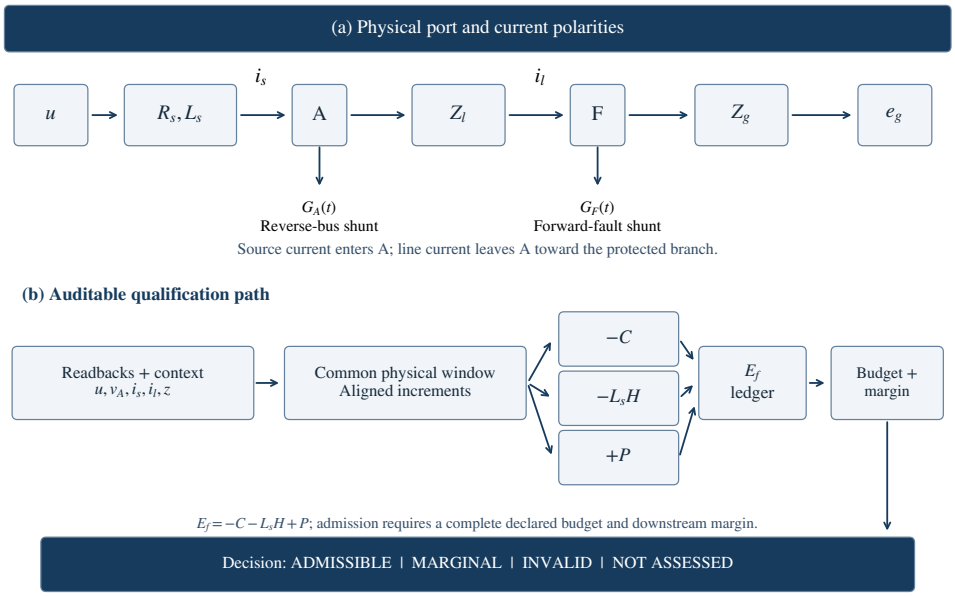

Fig. 5 Physical ports and auditable qualification path. The upper panel fixes the source-current and line-current polarities and distinguishes the reverse-bus and forward-fault shunts. The lower panel aligns readbacks over one physical window, retains the coefficient-exchange, endpoint, and realized-actuation terms separately, and combines them in the residual ledger. Admission also requires a complete error budget and downstream margin; the state output is an interface qualification record, not a relay trip command.

4.2.2 Delayed coefficient telemetry

The illustrative controller has $z = qx$, $q = 0.2 + \mathrm{j}$, and

$$\tau_x \dot{x} = a - x, \qquad 0 \le a \le X, \quad 0 \le x \le X, \tag{9}$$

with $X = 3$. A received exact coefficient sample x_d is at most $\bar{\delta}_t$ old. Scalar comparison gives

$$\ell = x_d e^{-\bar{\delta}_t/\tau_x}, \qquad u = X - (X - x_d)e^{-\bar{\delta}_t/\tau_x}. \tag{10}$$

The set-membership view propagates a set that is guaranteed to contain the unknown coefficient rather than a point estimate [46, 47]. The interval (10) contains every current value reachable with an unknown age in $[0, \bar{\delta}_t]$ and any admissible input a. It uses no fault label, input history, or future trajectory. Its midpoint and half-width give $\widehat{z} = q(\ell + u)/2$ and $\eta = |q|(u - \ell)/2$. For comparison, the generic rate bound uses the stale center qx_d and radius $|q| \min(X, X\bar{\delta}_t/\tau_x)$. Both budgeted variants receive the same controller knowledge. A range-clipped, recentered rate interval provides a stronger same-information comparison and is additionally evaluated; gains over an uncentered rate disk must not all be attributed to dynamics.

Proposition 1 (Exchange uncertainty disk)**.** *For exact window weights, suppose* $|z_j - \widehat{z}_j| \le \eta_j$ *and* $|d_j - \widehat{d}_j| \le \delta_j$ *simultaneously throughout a window. Then the disk centered at* $\widehat{C} = \sum_j w_j(\widehat{z}_j - \widehat{z}_k)\widehat{d}_j$ *with radius*

$$Q = \sum_j |w_j| \big[(\eta_j + \eta_k)(|\widehat{d}_j| + \delta_j) + |\widehat{z}_j - \widehat{z}_k|\delta_j \big] \tag{11}$$

contains C*. No independence of measurement or coefficient errors is required.*

Proof Write $z = \widehat{z} + e_z$ and $d = \widehat{d} + e_d$. The difference of the products is $(e_{z,j} - e_{z,k})\widehat{d}_j + (\widehat{z}_j - \widehat{z}_k)e_{d,j} + (e_{z,j} - e_{z,k})e_{d,j}$. Multiplication by w_j and the triangle inequality give (11). □

This elementary perturbation bound is included for auditability, not mathematical novelty. Treating delayed telemetry as current sets $\eta = 0$ without justification and may falsely report zero uncertainty. At a switching jump, a finite smooth-rate assumption must be replaced by a valid mode or amplitude envelope.

4.2.3 Projected interval with a shared endpoint

A directional statistic uses a real projection of a complex correction rather than its entire disk. When $z = qx$ with real $x_j \in [\ell_j, u_j]$, the repeated endpoint can be handled explicitly. For fixed measured current and $|h| \le 1$, define

$$\alpha_j = q w_j \widehat{d}_j \ (j < k), \qquad \alpha_k = -\sum_{j<k} \alpha_j. \tag{12}$$

In (12) the current-sample term cancels exactly; the endpoint occurs only through α_k. With $m_j = (\ell_j + u_j)/2$ and $r_j = (u_j - \ell_j)/2$, the interval for $\Re(hC)$ is centered at $c_h = \sum_j \Re(h\alpha_j)m_j$. For noiseless current its radius is

$$R_h = \sum_j |\Re(h\alpha_j)| r_j. \tag{13}$$

This is the exact support-function radius for the independent scalar box. It is not asserted tight for the smaller set of dynamically linked coefficient histories. With $|d_j - \widehat{d}_j| \le \delta$, a valid additional radius is

$$R_n = |hq|\delta \sum_{j<k} |w_j| \max\{|u_j - \ell_k|, |\ell_j - u_k|\}. \tag{14}$$

To verify (13), maximize a linear real function over each scalar interval independently. For (14), bound each omitted current-error product by the largest feasible $|x_j - x_k|$. Small-window corner enumeration and bounded-noise adversarial tests accompany the implementation.

4.2.4 From a budget to an engineering decision

An exchange-consistency budget can be allocated in voltage units before deployment. After applying an estimated correction $\widehat{C}$, the interval for the residual projection $\Re[h(C-\widehat{C})]$ has center $c_h - \Re(h\widehat{C})$ and the same radius $R_h + R_n$. The disk bound Q is already centered on the corresponding correction error. Neither requires adding the already-corrected exchange magnitude again. Actuator readback, sensor calibration, prefault estimation, impedance uncertainty, and quadrature error require their own allocations. Missing allocations yield "not assessed", rather than a falsely precise pass.

For an independently justified statistic $S = \Re(e^{-\mathrm{j}\phi} V I^*)$, with real ϕ, voltage error ϵ_V, and current error ϵ_I, the standard bilinear radius is

$$R_S = \epsilon_V |\widehat{I}| + \epsilon_I |\widehat{V}| + \epsilon_V \epsilon_I. \tag{15}$$

A nonzero sign is guaranteed invariant under (15) if $|\widehat{S}| > R_S$; otherwise this sufficient bound is inconclusive. This establishes agreement with the specified physical statistic under simultaneous bounds. It does not establish that the statistic correctly classifies the fault. Empty data windows, invalid bounds, a zero polarizing current, or missing actuator information must not generate a protection permission.

4.3 A distinct physical direction condition

For the balanced test network, the physical sign can be related to passive branch impedances under explicit topology assumptions. Write $Z_b = R_b + \mathrm{j}\omega L_b$ and $G_b = \mathcal{F}[\dot{d}_b] - \mathrm{j}\omega D_b$ for the source, line, and remote branches. For a forward fault with unchanged local shunt g_A, Kirchhoff's current law (KCL) gives $D_s = D_l + g_A V$. Substitution into the source ledger, with $K = Z_s + z_k$, gives

$$V = -\frac{K}{1 + g_A K} D_l + \epsilon_f, \tag{16}$$

$$\epsilon_f = \frac{P - C - L_s G_s}{1 + g_A K}. \tag{17}$$

For a reverse bus fault with unchanged remote shunt g_F and unchanged remote source voltage, the remote and line equations instead give

$$V = K_r D_l + \epsilon_r, \quad K_r = Z_l + \frac{Z_g}{1 + g_F Z_g}, \tag{18}$$

$$\epsilon_r = L_l G_l - \frac{L_g G_g}{1 + g_F Z_g}. \tag{19}$$

Assume the unchanged shunts g_A, g_F are real nonnegative conductances and the virtual coefficient satisfies $\Im(Z_s + z_k) > 0$. Positive branch resistance and inductance then give $\Im K_r > 0$, while $\Im K > 0$ follows from the explicit virtual-coefficient assumption.

Thus $S = \Im(V D_l^*)$ is negative for the forward case if

$$\frac{\Im K}{|1 + g_A K|^2} |D_l|^2 > |\epsilon_f| \, |D_l|, \tag{20}$$

and positive for the reverse case if $\Im K_r |D_l|^2 > |\epsilon_r| \, |D_l|$. The forward and reverse branch relations are (16) and (18), and the resulting forward sufficient condition is (20). These sufficient conditions follow by bounding the remainder projection. They are distinct from the inter-implementation agreement bound: they explicitly use the network topology and unchanged-side conditions. A local load change or remote source variation requires extra terms and invalidates an unmodified use of these relations.

These are analytical sufficient conditions for the stated dynamic branch model. The numerical study below uses a quasi-steady external network and therefore does not validate the remote-branch derivative terms or these fault-direction conditions. A realizable certificate additionally requires observable inputs and a bound on sampling remainders.

4.4 Numerical Verification Design

4.4.1 Physical model and operating point

The source branch is integrated in synchronous coordinates as

$$L_s \dot{i}_s = u - v_A - (R_s + \mathrm{j}\omega L_s) i_s. \tag{21}$$

Define $Z_s = R_s + \mathrm{j}\omega L_s$. Here $R_s = 0.04$ p.u., $\omega L_s = 0.22$ p.u., and frequency is 50 Hz. The external network is a quasi-steady nodal admittance model with four buses, three series branches and resistive shunts; the meshed variant adds a fourth branch. An inserted fault bus splits the selected branch. The external grid-equivalent branch reactance is 0.5/SCR p.u., where SCR denotes short-circuit ratio; it is distinct from the fixed converter source-branch reactance ωL_s. The retained code specifies the admittance matrices and shunts. This hybrid model retains source-inductor dynamics but not external-line electromagnetic transients.

The prefault current is $0.45 e^{\mathrm{j}\theta}$ p.u.; the network solution gives v_0 and $u_0 = v_0 + (R_s + \mathrm{j}\omega L_s) i_0$. The controller command is $u_0 - z(i_s - i_0)$, with an 8-ms first-order coefficient response toward $(0.18 + 0.55\mathrm{j}) \min(|i_s|, 1.5)$. A command-level current limiter targets 1.5 p.u. and the applied voltage is limited to 1.2 p.u. These command limits do not guarantee transient terminal-current or terminal-voltage bounds. The realized incremental actuation is $p = (u - u_0) + z(i_s - i_0)$.

4.4.2 Finite grid and numerical checks

The grid contains 108 physical configurations: radial/meshed topology, SCR $\{1.5, 2.5, 5\}$, resistance $\{0.01, 0.1\}$ p.u., location $\{0.2, 0.5, 0.8\}$, and three equivalent fault-admittance severities. The retained labels 3ph, LL and LG denote resistance multipliers $1, 1.8, 3$; the latter two are positive-sequence proxies, not phase-resolved fault validation. Radial SCR=2.5 is the calibration-labelled stratum and is excluded

from held-out strata. Five common rotations test equivariance; ages $\{0.1, 0.5, 1\}$ ms are measurement conditions. These produce 1620 distinct records without overlapping physical strata.

An event-aligned Heun solver uses 0.1-ms steps. The window spans 5–25 ms after fault inception, entirely before clearing. Synchronous increments and actuation are multiplied by $e^{\mathrm{j}\omega t}$ before stationary-frame demodulation. A separately restated right-hand side integrated with adaptive DOP853 supplies a numerical reference for step refinement; shared topology and admittance routines limit this to same-model numerical verification.

4.4.3 Metrics, denominators and retained failures

The revised protocol is exploratory because it follows inspection of the earlier implementation. Physical-domain rates weight each physical tuple once. The full time history must satisfy $|i_s| \leq 1.5$ and $|v_A| \leq 1.2$ p.u. Violations are retained and force INVALID. Numerical closure coverage uses the stated 0.005-p.u. tolerance. Conditional residual summaries use only domain-valid tuples at zero rotation and the smallest telemetry age; phase/age repetitions are not additional independent units. This deterministic grid supports descriptive medians and ranges, not population confidence intervals. Every baseline is computed as the magnitude of its complete complex residual. In particular, summing component magnitudes is not a frozen-product baseline.

In the physical sweep, a complete interface error budget and an independently calibrated downstream decision margin are unavailable. Domain-valid records are therefore NOT_ASSESSED; no permission is inferred from numerical closure or a pointwise coefficient-drift diagnostic. Interface-state semantics and the declared error-budget components are listed in Supplementary Tables S1 and S2. A separate scalar-controller experiment tests interval containment and state transitions with a defined voltage-projection margin. This keeps the measured quantity and its error radius in the same units.

4.4.4 Follow-up source-current domain governor

A separate ideal-feedforward follow-up uses the same physical grid and ledger audit with a source-current domain governor. The protocol is retained separately from the original sweep. During the fault interval, the governor measures v_A and i_s and applies

$$u_{\mathrm{des}} = v_A + Z_s i_s - k_g L_s (i_s - i_{s,\mathrm{pre}}), \tag{22}$$

with $k_g = 300\ \mathrm{s}^{-1}$, followed by the same 1.2-p.u. voltage magnitude limit. Prefault operation remains at the original equilibrium. In the unsaturated regime, substitution into the source equation yields

$$\frac{\mathrm{d}}{\mathrm{d}t}(i_s - i_{s,\mathrm{pre}}) = -k_g (i_s - i_{s,\mathrm{pre}}). \tag{23}$$

Thus, with the initialized equilibrium, $i_s = i_{s,\mathrm{pre}}$ is preserved by construction. The implementation uses exact instantaneous v_A and i_s, exact source parameters, and prescribed fault-on/fault-off times. It does not include fault detection, sensor delay or noise, parameter mismatch, switching actuation, or a fault-current-support requirement. The variant is an ideal feasibility benchmark for the interface audit; its domain coverage is not evidence of a deployable robust fault controller.

4.4.5 Causal sampled-data sensitivity follow-up

A new exploratory protocol was fixed after inspecting the ideal governor results and before executing this follow-up. It evaluates the same 108 physical tuples at zero rotation, without duplicating the coefficient-telemetry ages. Controller activation uses a local detector $|\widehat{v}_A - v_{A,\mathrm{pre}}| > 0.05$ p.u., with the profile-specific additional delay. The detector latches until the simulation ends; neither the fault label nor the known fault-on/off times selects the control mode. The plant alone uses those times to apply its physical fault.

The control command is sampled and held every 0.1 ms. Both voltage and current readbacks have a shared delay of 0, 0.1 or 0.5 ms. A deterministic 137-Hz complex perturbation of magnitude at most 0.01 p.u. tests bounded sensor error at phases zero and $\pi/2$; the current perturbation equals j times the voltage perturbation, so errors are fully correlated. These are a finite sensitivity family, not arbitrary independent bounded errors or stochastic replications. Estimated source resistance and inductance are jointly scaled by 0.9 or 1.1 to represent parameter mismatch, while the physical plant is unchanged. The magnitude-limited voltage command can pass through a first-order actuator with time constant 0.2 or 0.5 ms. An additional 2-ms detector delay tests late activation. The combined condition uses 0.1-ms readback delay, 0.01-p.u. sensor perturbation, +10% impedance error, 0.2-ms actuator lag and 0.5-ms additional detection delay. A final condition keeps these imperfections but requests a 0.9-p.u. current magnitude along the prefault phase, instead of 0.45 p.u.; this is a current-support stress test, not grid-code compliance.

All ten conditions are evaluated at both perturbation phases over every tuple. Domain classification uses the full 80-ms sampled history, including inception and clearing, and requires both phase conditions to satisfy the original limits. Clipping fractions, detector latencies and fault-interval tracking errors are retained as secondary diagnostics. No failed domain is excluded. The combined condition is additionally recomputed with 0.05-ms plant-integration steps on all tuples and both phases, while command updates and detector/readback sampling remain fixed at 0.1 ms. The protocol, source hashes, complete attempt denominator and scenario records are supplied separately from the earlier ideal study.

4.4.6 Independent phase-domain stress audit

A separately implemented three-phase averaged RL-C circuit is used as an exploratory structural stress audit, not as a calibrated validation of the preceding quasi-steady external-network model. It retains dynamic source and line currents, shunt bus capacitances, and explicit 3ph, phase-to-ground (LG), and phase-to-phase (LL) fault admittances. The 54 complete combinations cross SCR $\{1.5, 2.5, 5\}$, fault resistance

$\{0.01, 0.1\}$ p.u., location $\{0.2, 0.5, 0.8\}$, and the three fault types. A type-stratified hash split assigns 36 tuples to gain selection and 18 to one held-out comparison. Gain is selected from $\{0, 75, 150, 300, 450\}$ s^{-1} by training-domain retention, with ties resolved toward the smaller gain; held-out cases compare that gain with zero gain on identical inputs. Six nonfault events test local-detector selectivity. The circuit is propagated by matrix exponentials at 2- μs output intervals; a representative held-out case is repeated at 1 μs. The frozen protocol and all attempts are reported separately. Because the circuit is not calibrated to a vendor model or hardware, this audit measures model-conditional stress behavior and cannot establish field performance or replace EMT, CHIL, or hardware validation.

4.4.7 Separate bounded-telemetry mechanism experiment

This experiment instantiates (9) with $\tau_x = 2$ ms, $X = 3$, and $q = 0.2 + \mathrm{j}$; it is distinct from the 8-ms network controller. Five initial states $\{0, 0.3, 1.5, 2.7, 3\}$ are crossed with 13 piecewise-constant input profiles: zero, maximum, step, alternating, sampled sine, and eight fixed-seed uniform profiles. Input segments last 0.25 ms and scalar trajectories use the exact exponential solution. A prescribed rotating current is sampled with the same 20-ms normalized trapezoidal window at 0.1-ms steps. Coefficient and current noise bounds independently take $\{0, 0.01, 0.05\}$, with bounded deterministic perturbations retained in the code. Ages are $\{0.1, 0.5, 1, 2, 5, 10\}$ ms in the primary grid. All methods receive the same noisy aged readbacks, current, age bound and controller constants; clean trajectories are used only for scoring. No correction and a stale point estimate provide unbudgeted diagnostic comparisons, while both certified-bound variants use the merged-endpoint projection.

The declared projection-error allocation is 0.05 p.u. and the synthetic nominal margin is 0.02 p.u. A radius above the allocation is INVALID; a radius within allocation but at least the margin is MARGINAL; a smaller radius is ADMISSIBLE for this exchange-only diagnostic. A false-safe event denotes hypothetical acceptance with absolute correction error at least the synthetic margin, not an observed trip error. After the primary grid yielded no admissible conditions, an exploratory grid used ages $\{0, 0.01, 0.025, 0.05, 0.075, 0.1\}$ ms, retaining all other settings. Its plan and outputs are separately identified.

4.4.8 Software and reproducibility

The retained numerical implementation uses Python, NumPy, SciPy and Matplotlib; exact dependency versions are supplied in `requirements.lock.txt`. Every reported number is recomputed by the retained executable code from the frozen scenario records, so the results are reproducible independently of the drafting process. AI tools were used only for language translation and polishing.

Data availability

Scenario-level numerical records, protected unit tests, deterministic figure-generation code and reproduction instructions are provided as Supplementary Information and in

the retained reproduction package described in the Methods. The complete package, including per-tuple records and source hashes, is available to editors and referees during peer review, from the corresponding author on reasonable request, and will be deposited in a public repository upon publication. No third-party dataset was used.

Author contributions

S.F. designed the study, derived the interface ledger, developed and validated the numerical implementation, performed the audits, prepared the figures, and wrote and revised the manuscript. Y.F. defined the industrial field context and engineering requirements, assessed the engineering interpretability of the results, and reviewed and revised the manuscript.

Competing interests

The authors declare the following competing interests: this work was supported by the XJ Group Corporation research project "Development of a DC Ultra-High-Speed Line Protection Device" (Project No. 2020G001), and Y.F. is an employee of XJ Electric Co., Ltd., a manufacturer of power-system protection and control equipment. The manuscript reports model-conditional numerical simulations only and contains no product-specific data, vendor device model, or commercial performance claim. S.F. declares no competing interests.

Ethics declaration

This study does not involve human participants, human data, or animals; institutional review board approval and informed consent are not applicable.

Acknowledgements

This work was supported by the XJ Group Corporation research project "Development of a DC Ultra-High-Speed Line Protection Device" (Project No. 2020G001). Author identifiers: S.F. https://orcid.org/0009-0001-8772-2449; Y.F. https://orcid.org/0009-0001-0819-8387.

References

[1] Fan, B., Liu, T., Zhao, F., Wu, H., Wang, X.: A Review of Current-Limiting Control of Grid-Forming Inverters Under Symmetrical Disturbances. IEEE Open Journal of Power Electronics **3**, 955–969 (2022) https://doi.org/10.1109/ojpel.2022.3227507

[2] Baeckeland, N., Chatterjee, D., Lu, M., Johnson, B., Seo, G.-S.: Overcurrent Limiting in Grid-Forming Inverters: A Comprehensive Review and Discussion. IEEE Transactions on Power Electronics **39**(11), 14493–14517 (2024) https://doi.org/10.1109/tpel.2024.3430316

[3] Johansson, H., Xing, Q., Taylor, N., Wang, X.: Impacts of grid-forming inverters on distance protection. IET Generation, Transmission & Distribution **19**(1) (2025) https://doi.org/10.1049/gtd2.13354

[4] Li, Y., Wu, H., Wang, X.: Impact of Grid-Forming Inverters on Protective Relays: A Perspective for Current Limiting Control Design. IEEE Transactions on Industrial Electronics **73**(2), 2116–2127 (2026) https://doi.org/10.1109/tie.2025.3594454

[5] Akuhwa, F., Green, T.C.: Impact of inverter and grid conditions on impedance estimation of distance protection in grid-following and grid-forming inverter systems. In: IET Conference Proceedings, vol. 2026, pp. 333–338. Institution of Engineering and Technology (IET), Stevenage, UK (2026). https://doi.org/10.1049/icp.2026.2228

[6] Xing, Q., Johansson, H., Wang, X., Taylor, N., Li, Y.: Impact of grid forming inverter settings on distance protection overreach. In: IET Conference Proceedings, vol. 2025, pp. 204–210. Institution of Engineering and Technology (IET), Stevenage, UK (2025). https://doi.org/10.1049/icp.2025.0471

[7] Saifussalam, M., Rahman, F.S., Hariyanto, N.: Distance protection performance of transmission lines influenced by inverter-based resources. 2024 6th International Conference on Power Engineering and Renewable Energy (ICPERE), 1–6 (2024) https://doi.org/10.1109/icpere63447.2024.10845737

[8] Chen, X., Bu, S., Haddadi, A., Kocar, I.: Performance of distance protection under inverter-based resources with IEEE 2800 current injection requirements. In: IET Conference Proceedings, vol. 2025, pp. 577–582. Institution of Engineering and Technology (IET), Stevenage, UK (2025). https://doi.org/10.1049/icp.2025.0585

[9] Liu, D., Hong, Q., Cao, S., Dyśko, A., Xu, L., Booth, C.: Impact of converters' negative-sequence fault current injection on distance protection. In: IET Conference Proceedings, vol. 2025, pp. 445–450. Institution of Engineering and Technology (IET), Stevenage, UK (2025). https://doi.org/10.1049/icp.2025.0542

[10] Wu, C., Liu, X., Judge, P.D.: Impact of a power converter virtual impedance based fast fault current injection control strategy on distance protection. In: IET Conference Proceedings, vol. 2024, pp. 235–240. Institution of Engineering and Technology (IET), Stevenage, UK (2024). https://doi.org/10.1049/icp.2024.0987

[11] Benjamin, J., SAHOO, A.K., Bhui, P.: Enhanced fault current utilization by grid-forming inverter using non-linear transient virtual resistance during symmetrical faults (2025) https://doi.org/10.36227/techrxiv.174552887.73928983/v1

[12] You, F., Wang, Y., Zhao, Z., Chao, C., Wu, M., Ding, L., Zhao, X., Han, Z., Liu, Z., Hou, Y., Zheng, X.: Grid code compliant fault current limiting strategy for grid-forming inverter-based resource. IET Conference Proceedings **2025**, 483–488

(2026) https://doi.org/10.1049/icp.2025.3879

[13] Cao, Y., Sun, G., Lu, J., Li, D., Wang, X., Ukil, A., Swain, A.: Post-fault transient enhancement based on adaptive power-angle resetting for grid-forming inverter with current limiting considering phase jumping along with fault clearance. IEEE Transactions on Power Electronics, 1–16 (2026) https://doi.org/10.1109/tpel.2026.3730765

[14] Azizi, A., Banaiemoqadam, A., Hooshyar, A., Patel, M.: A Blind Spot in the LVRT Current Requirements of Modern Grid Codes for Inverter-Based Resources. IEEE Transactions on Power Delivery **38**(1), 319–334 (2023) https://doi.org/10.1109/tpwrd.2022.3187223

[15] Liu, X., Judge, P., Leterme, W., Chaffey, G., Van Hertem, D.: Contrasting the requirements on MMC control for grid code compliance and distance protection. In: IET Conference Proceedings, vol. 2024, pp. 101–106. Institution of Engineering and Technology (IET), Stevenage, UK (2024). https://doi.org/10.1049/icp.2024.0883

[16] Daryabar, H., Abedini, M., Davarpanah, M.: An adaptive K-factor control scheme for inverter-based resources to enhance operation of distance protection. International Journal of Electrical Power & Energy Systems **173**, 111349 (2025) https://doi.org/10.1016/j.ijepes.2025.111349

[17] Shamseh, M.B., Haiqing, L.: Adaptive virtual impedance for reactive current control during fault conditions in grid-forming inverters. 2024 IEEE Applied Power Electronics Conference and Exposition (APEC), 2251–2257 (2024) https://doi.org/10.1109/apec48139.2024.10509488

[18] Li, X., Zhu, R.: Transient stability analysis of grid-forming converter embedding adaptive virtual impedance as current limiting strategy. 2024 2nd Power Electronics and Power System Conference (PEPSC), 95–100 (2024) https://doi.org/10.1109/pepsc63375.2024.10823469

[19] Yang, Z., Chen, X., Javid, Z., Kocar, I.: Enhanced fault response and efficient fault analysis of grid-forming converters with virtual impedance control (2025) https://doi.org/10.2139/ssrn.5113685

[20] Wang, P., Wang, P., Wu, H., Hao, W., Wang, W., Xu, D.: An improved current-limiting control strategy of grid-forming inverter during grid fault. 4th International Conference on Information Science, Electrical, and Automation Engineering (ISEAE 2022), 84 (2022) https://doi.org/10.1117/12.2640195

[21] Chao, C., Zheng, X., Weng, Y., Liu, Y., Gao, P., Tai, N.: Adaptive Distance Protection Based on the Analytical Model of Additional Impedance for Inverter-Interfaced Renewable Power Plants During Asymmetrical Faults. IEEE Transactions on Power Delivery **37**(5), 3823–3834 (2022) https://doi.org/10.

1109/tpwrd.2021.3138128

[22] Xie, Y., Zou, X., Duan, M., Fan, F., Wang, H., Liu, Y.: Distance Protection for Lines Terminated by Inverter-Based Resources Compatible With Various Inverter Control Schemes. IEEE Transactions on Industrial Electronics **72**(12), 13151–13163 (2025) https://doi.org/10.1109/tie.2025.3577310

[23] Yang, Z., Zhang, Q., Liao, W., Bak, C.L., Chen, Z.: Harmonic Injection Based Distance Protection for Line With Converter-Interfaced Sources. IEEE Transactions on Industrial Electronics **70**(2), 1553–1564 (2023) https://doi.org/10.1109/tie.2022.3159971

[24] Adhikari, P., Brahma, S., Gadde, P.H.: Source-Agnostic Time-Domain Distance Relay. IEEE Transactions on Power Delivery **37**(5), 3620–3629 (2022) https://doi.org/10.1109/tpwrd.2021.3133333

[25] Cai, Y., Qin, W., Zhu, Z., Lu, R., Zhao, K., Yan, Z.: Active distance protection schemes for asymmetrical faults of renewable energy stations transmission line. International Journal of Electrical Power & Energy Systems **177**, 111818 (2026) https://doi.org/10.1016/j.ijepes.2026.111818

[26] Huang, L., Wu, C., Zhou, D., Blaabjerg, F.: A Power-Angle-Based Adaptive Overcurrent Protection Scheme for Grid-Forming Inverter Under Large Grid Disturbances. IEEE Transactions on Industrial Electronics **70**(6), 5927–5936 (2023) https://doi.org/10.1109/tie.2022.3199906

[27] Li, W., Zhang, Y., Feng, Q.: Overcurrent protection of grid forming converter during fault recovery stage with virtual impedance. 2026 8th Asia Energy and Electrical Engineering Symposium (AEEES), 258–264 (2026) https://doi.org/10.1109/aeees69423.2026.11556837

[28] Baeckeland, N., Venkatramanan, D., Dhople, S., Kleemann, M.: On the Distance Protection of Power Grids dominated by Grid-forming Inverters. In: 2022 IEEE PES Innovative Smart Grid Technologies Conference Europe (ISGT-Europe), pp. 1–6. IEEE, Piscataway, NJ, USA (2022). https://doi.org/10.1109/isgt-europe54678.2022.9960410

[29] Lopes, F.V., Davi, M.J.B.B., Oleskovicz, M., Hooshyar, A., Dong, X., Neto, A.A.A.: Maturity Analysis of Protection Solutions for Power Systems Near Inverter-Based Resources. IEEE Transactions on Power Delivery **39**(5), 2630–2643 (2024) https://doi.org/10.1109/tpwrd.2024.3420421

[30] Li, Y., Wu, H., Wang, X.: A Protection-Interoperable Fault Ride-Through Control for Grid-Forming Inverters. IEEE Transactions on Industrial Electronics **73**(2), 2415–2426 (2026) https://doi.org/10.1109/tie.2025.3610752

[31] Wang, K., Lin, X., Wei, F., Li, Z., Gao, J., Weng, H.: Enhancing Superimposed-Based Distance Protection in Inverter-Dominated Grids Based on Control-Protection Coordination. IEEE Transactions on Industrial Electronics **73**(2), 2092–2103 (2026) https://doi.org/10.1109/tie.2025.3594449

[32] Chao, C., Zheng, X., Weng, Y., Liu, Z., Ye, H., Liu, H., Zhang, H., Liu, Y., Wang, Y., Tai, N.: Collaborative Solution of Distance Protection and Dual Current Control for Outgoing Lines of Inverter-Based Resources During Line-to-Line Faults. IEEE Transactions on Smart Grid **15**(4), 3782–3794 (2024) https://doi.org/10.1109/tsg.2024.3369767

[33] Qian, K., Wen, M., Xue, X., Sun, Z.: A Novel Directional Element for AC Lines in Systems with Inverter-Based Resources. Sensors **26**(10), 2991 (2026) https://doi.org/10.3390/s26102991

[34] Song, H., Gao, H., Guo, Y., Peng, F., Yuan, T., Zhou, J.: A novel directional pilot protection for outgoing lines of grid-forming inverter based resources. In: IET Conference Proceedings, vol. 2026, pp. 145–150 (2026). https://doi.org/10.1049/icp.2026.1863

[35] Liu, S., Wu, J., Zhang, Y., Zheng, R.: A Novel Control-Protection Coordination Strategy of Power Lines Connected with Inverter-Based Resources. Energy Engineering **123**(6), 1–10 (2026) https://doi.org/10.32604/ee.2026.081082

[36] Ebrahimi, E., Sanjari, M.J., Gharehpetian, G.B.: Control of three-phase inverter-based DG system during fault condition without changing protection coordination. International Journal of Electrical Power & Energy Systems **63**, 814–823 (2014) https://doi.org/10.1016/j.ijepes.2014.05.058

[37] Alwan, N., Papic, V.: Phasor estimation of transient electrical signals using modified covariance enhanced cleaned characteristic harmonic filtering in protection relay. Energies **19**, 711 (2026) https://doi.org/10.3390/en19030711

[38] Gajic, Z., Zubic, S., Kockott, M.: Phasor-based transient earth-fault protection. 2021 74th Conference for Protective Relay Engineers (CPRE), 1–26 (2021) https://doi.org/10.1109/cpre48231.2021.9429719

[39] Romaniuk, F.A., Rumiantsev, Y.V., Rumiantsev, V.Y., Novash, I.V.: Compensation of Dynamic Phase Error in the Formation of Orthogonal Components of Input Signals in Microprocessor Protections. ENERGETIKA Proceedings of CIS higher education institutions and power engineering associations **65**(3), 197–208 (2022) https://doi.org/10.21122/1029-7448-2022-65-3-197-208

[40] Chowdhury, R., Sun, C., Taylor, D.: Review of sir calculations for distance protection and considerations for inverter-based resources (2023) https://doi.org/10.36227/techrxiv.24047445

[41] Reis, R.L.A., Lopes, F.V., Leite, E.J.S., Zat, G., Souza, J.V., Scheid, A., Jahn, T.G.: Evaluation of single-ended impedance-based transmission fault location using fixed and variable window phasor estimation approaches. Electric Power Systems Research **223**, 109571 (2023) https://doi.org/10.1016/j.epsr.2023.109571

[42] Mobashsher, M.M., Hosseini, S.M., Abdoos, A.A., Hashemi, S.M., Sanaye-Pasand, M., Mehrjerdi, H.: A new fault location scheme based on local measurements for transmission lines connected to inverter-based resources. Electric Power Systems Research **228**, 110079 (2024) https://doi.org/10.1016/j.epsr.2023.110079

[43] Aboshady, F.M., Thomas, D.W.P., Sumner, M.: A new single end wideband impedance based fault location scheme for distribution systems. Electric Power Systems Research **173**, 263–270 (2019) https://doi.org/10.1016/j.epsr.2019.04.034

[44] Baayeh, A.G., Kleemann, M.: Fast time-domain fault location for distance protection in inverter-based networks. In: IET Conference Proceedings, vol. 2025, pp. 98–104. Institution of Engineering and Technology (IET), Stevenage, UK (2025). https://doi.org/10.1049/icp.2025.1052

[45] Sanders, S.R., Noworolski, J.M., Liu, X.Z., Verghese, G.C.: Generalized averaging method for power conversion circuits. In: 21st Annual IEEE Conference on Power Electronics Specialists, pp. 333–340 (1990). https://doi.org/10.1109/PESC.1990.131207

[46] Zou, L., Wang, Z., Geng, H., Liu, X.: Set-membership filtering subject to impulsive measurement outliers: A recursive algorithm. IEEE/CAA Journal of Automatica Sinica **8**(2), 377–388 (2021) https://doi.org/10.1109/JAS.2021.1003826

[47] Qi, J., He, G., Mei, S., Liu, F.: Power system set membership state estimation. 2012 IEEE Power and Energy Society General Meeting, 1–7 (2012) https://doi.org/10.1109/pesgm.2012.6345728

[48] Belforte, G., Tay, T.T.: Recursive estimation algorithms for linear models with set membership error. Bounding Approaches to System Identification, 83–99 (1996) https://doi.org/10.1007/978-1-4757-9545-5_6

[49] Qing, H.: Set membership parameter estimation for linear systems subject to bounded disturbances. 2007 Chinese Control Conference, 337–340 (2006) https://doi.org/10.1109/chicc.2006.4347580

[50] Amairi, M.: Recursive set membership estimation for output–error fractional models with unknown–but–bounded errors. International Journal of Applied Mathematics and Computer Science **26**, 543–553 (2016) https://doi.org/10.1515/

amcs-2016-0038

[51] Harirchi, F., Ozay, N.: Guaranteed model-based fault detection in cyber–physical systems: A model invalidation approach. Automatica **93**, 476–488 (2018) https://doi.org/10.1016/j.automatica.2018.03.040

[52] Taylor, J.A., Domínguez-García, A.D.: Active Fault Detection in Static Systems. IEEE Transactions on Automatic Control **70**(8), 5523–5529 (2025) https://doi.org/10.1109/tac.2025.3547848

Supplementary Files

This is a list of supplementary files associated with this preprint. Click to download.

- 02Supplementary.pdf
- 05Supplementarysource.zip